Domain structure and reorientation in $CoFe_2O_4$

M. Abes,[1,*] C. T. Koops,[1] S. B. Hrkac,[1] J. McCord,[2] N. O. Urs,[2] N. Wolff,[2] L. Kienle,[2] W. J. Ren,[3] L. Bouchenoire,[4,5]
B. M. Murphy,[1,6,†] and O. M. Magnussen[1,6]
[1]*Institute for Experimental and Applied Physics, Kiel University, D-24098 Kiel, Germany*
[2]*Institute for Materials Science, University of Kiel, D-24143 Kiel, Germany*
[3]*Shenyang National Laboratory for Materials Science, Institute of Metal Research, Chinese Academy of Sciences, Shenyang 110016, People's Republic of China*
[4]*XMaS, European Synchrotron Radiation Facility, F-38000 Grenoble, France*
[5]*Department of Physics, University of Liverpool, Liverpool L69 7ZE, United Kingdom*
[6]*Ruprecht Haensel Laboratory, Kiel University, D-24098 Kiel, Germany*
(Received 14 December 2015; revised manuscript received 20 April 2016; published 18 May 2016)

The microscopic processes underlying magnetostriction in ferrites were studied for the case of $CoFe_2O_4$ single crystals by high-resolution *in situ* x-ray diffraction and complementary magnetic microscopy techniques. The data support the reports of Yang and Ren [Phys. Rev. B **77**, 014407 (2008)] that magnetostriction in these materials originates from the switching of crystallographic domains, similar to ferroelastic or ferroelectric domain switching, and reveals the presence of two coexisting tetragonal spinel structures, corresponding to domains of high and of low strain. The latter alternate in the crystal, separated by 90° domain boundaries, and can be explained by the effect of internal stress emerging during the transition into the ferrimagnetic phase. During magnetization of the sample two structural transitions are observed: a conversion of the transversal into axial domains at 1.95 kOe and a growth of the high-strain domains at the cost of the low-strain axial domains at 2.8 kOe. These microscopic changes are in good agreement with the macroscopic magnetization and magnetostriction behavior of $CoFe_2O_4$.

DOI: 10.1103/PhysRevB.93.195427

I. INTRODUCTION

The ferrimagnetic material cobalt ferrite ($CoFe_2O_4$, CFO) possesses a large saturation magnetostriction (λ_S) in the range of 3–12 $\times 10^{-4}$, which aroused interest for advanced technology applications and fundamental research [1–3]. Specifically, this large magnetostriction favors CFO and related ferrites as the sensor and actuator component in devices, where the coupling of the magnetization with the magnetostriction is employed [4–7]. For example, the change in the magnetization and the magnetic anisotropy induced by applying a mechanical stress [8] can be utilized in composites of the ferrimagnet CFO with a ferroelectric material [e.g., $Pb(Zr, Ti)O_3$ (PZT) [9], $[PbMg_{1/3}Nb_{2/3}O_3]_{0.68} - [PbTiO_3]_{0.32}$ (PMN-PT) [10], or $BaTiO_3$ [11]], where these magnetic properties can be coupled to an electric field via elastic interactions at the CFO-ferroelectric interface [12–14]. Such composites have been found to exhibit a large magnetoelectric response [15] that depends on the microstructure, the elastic coupling across the interface, and, most importantly, on the magnetostrictive behavior of CFO [16].

Although CFO and other ferrites have been studied for a long time [1,3,10–14,17–19], a microscopic model describing the magnetostrictive behavior is still missing. Previous studies of well-defined single crystals focused on the macroscopic magnetic anisotropy and magnetostriction [1,18], which require detailed modeling of the entire measured system and rely strongly on assumptions regarding the homogeneity of the geometrical and material properties and the precise values of the elastic parameters. However, they did not provide detailed insights into the domain structure and the domain reorientation in magnetic fields, which is of central importance for a complete understanding of the magnetostriction behavior. Recently, Yang and Ren demonstrated by high-resolution diffraction studies that the structural and magnetic domains are strongly coupled in CFO and other magnetostrictive materials [17]. Specifically, they showed that in the ferrimagnetic room temperature phase CFO crystallizes in an inverse spinel structure with tetragonal symmetry (space group $I4_1/amd$, $a = b = 8.388$ Å, and $c = 8.378$ Å) in a state below the Curie temperature T_c. In this structure the cubic crystal lattice (space group $Fd\text{-}3m$, $a_0 = 8.385$ Å) of the paramagnetic state above $T_c (T_c = 760\,\text{K})$ is slightly distorted. This lowered crystal symmetry is associated with the magnetostriction effect in which the magnetic moment is—similar to the electric polarization in ferroelectric materials—coupled to the crystal lattice, inducing the distortion in the crystal lattice.

Because of this coupling of structural and magnetic domains, the paramagnetic to ferrimagnetic phase transition as well as the magnetostriction behavior itself should involve significant internal stresses. While in ferroelectrics stress evolution and domain micromechanics have been the subject of intense recent studies [20,21], detailed studies of the domain structure and dynamics in magnetostrictive materials are largely missing so far. In the present study, we report results of a study on single-crystalline CFO by a combination of high-resolution x-ray diffraction (XRD), magneto-optical Kerr effect (MOKE) microscopy, complementary transmission electron microscopy (TEM), and vibrating sample magnetometry (VSM) investigations, which provide direct insight into the field-dependent lattice structure and the magnetic domains.

---

[*] Present address: Department of Solid State Sciences, Ghent University, 9000 Ghent, Belgium.

[†] murphy@physik.uni-kiel.de

As we will show in the following, our data confirm and refine the picture proposed by Yang and Ren, and additionally allow us to clarify the complex and intertwined transitions of the structural and magnetic domains in this material.

II. EXPERIMENTAL

The bulk CFO single crystals were grown using a flux method [22,23] where $Na_2B_4O_7 \cdot 10H_2O$ (borax) was utilized as the flux. Co_3O_4 and Fe_2O_3 were used as the starting materials. These materials were mixed together with borax and put in a tightly closed Pt crucible. The setup was subsequently heated from room temperature to 1370 °C at a rate of 100 °C/h, held there for 6 h, then slowly cooled down to 990 °C at 2 °C/h, and finally cooled by switching off the furnace power supply. The single crystals have an octahedron shape with $\langle 111 \rangle$ facets of approximately $2 \times 2 \times 2\,\mathrm{mm}^3$ size.

The XRD measurements were performed at the bending magnet beamline XMaS, the UK-CRG [24] at the European Synchrotron Radiation Facility (ESRF) in France, and at beamline I16 of the Diamond Light Source (DLS) in the United Kingdom. The photon energy was tuned to 15 keV on both beamlines. A Si(111) analyzer was utilized to increase the resolution in scattering vector q for the Bragg peak position analysis (resulting relative strain resolution $\varepsilon_r = 5 \times 10^{-5}$). The magnetic domain images were obtained with a magneto-optical Kerr microscope in longitudinal mode [25,26] and a FEI Tecnai F30 G² STwin TEM in Lorentz mode. The TEM sample was prepared by cutting the single crystal with a focused ion beam (FIB). The magnetization behavior of these samples was characterized by vibrating sample magnetometry (VSM). All studies were performed at room temperature, i.e., in the noncubic ferrimagnetic phase.

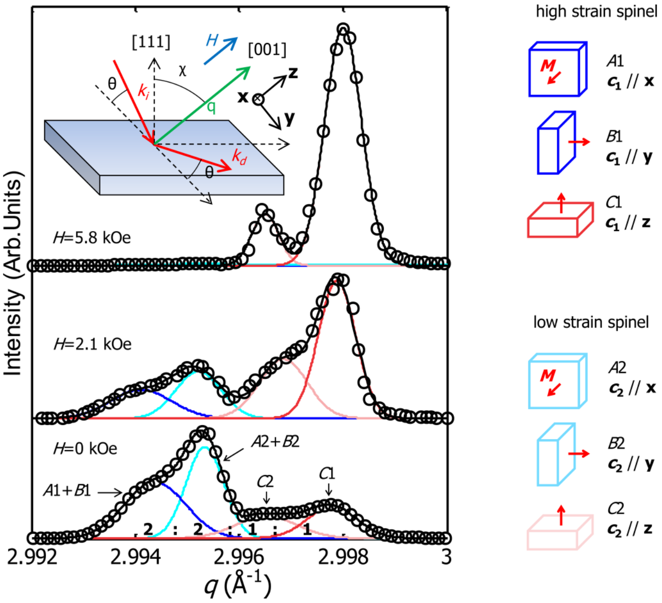

FIG. 1. Selected 2θ scans, taken from a series of measurements of the $\{400\}$ CFO Bragg peaks with increasing external magnetic field H. The data illustrate the noncubic crystal structure of CFO and show H-induced changes in the domain distribution. The data can be fitted by four Gaussian peaks (colored lines), corresponding to the axial ($C1$, $C2$) and transversal ($A1/B1$, $A2/B2$) oriented domains of two spinel phases, which are displayed on the right hand side of the figure. The inset shows the schematic illustration of the x-ray diffraction geometry. M is the magnetization vector of the sample.

III. RESULTS AND DISCUSSION

XRD studies reveal the high quality of the CFO single crystals used in this study. A series of XRD measurements was recorded at the $\{400\}$ CFO Bragg reflections as a function of an external magnetic field H, which was applied parallel to the x-ray scattering vector q (see the inset of Fig. 1). In the absence of the magnetic field the reflection is split into four peaks with an intensity ratio of 2:2:1:1 (Fig. 1). This behavior was observed in several measurements at different beamlines and is reproducible for three different samples. These features can be assigned to two differently distorted tetragonal spinel structures of which each exhibits three different domains that are oriented with the c axis along the $\langle 100 \rangle$ directions of the original cubic lattice (schematically illustrated at the right hand side of Fig. 1; **x**, **y**, and **z** denote the cubic lattice directions). Based on the intensity changes in the presence of a magnetic field (see below), the $A1/B1$, and $C1$ peaks can be identified as the Bragg reflections of a more strongly tetragonally distorted phase which we will call “high-strain spinel” hereafter, whereas the $A2$, $B2$, and $C2$ peaks can be assigned to a less distorted structure, denoted as “low-strain spinel.” These structures possess a similar cell volume V but their lattice distortion differs by a factor of 2 (see Table I). The domains $A1$, $B1$, $A2$, and $B2$ correspond to transversal domains (c axis of the spinel cell perpendicular to the scattering vector q) while the domains $C1$ and $C2$ correspond to axial domains (with the c axis parallel to q). The observed intensity ratio indicates an equal volume fraction of the six domain types at room temperature, i.e., an isotropic distribution of the domains along the symmetrically equivalent directions. Both of the ferrimagnetic unit cells are of inverse spinel structure with tetragonal symmetry (space group $I4_1/amd$) but with different lattice parameters due to the weak distortion of the cubic crystal lattice (space group $Fd\text{-}3m$) of the paramagnetic state. The lowered crystal symmetry caused by the tetragonal

TABLE I. Lattice constants (a and c), lattice distortion (ε), FWHM, and unit cell volume (V) obtained from our experiment in comparison to the data from Yang and Ren [17].

	a (Å)	c (Å)	a_0(Å)	ε	FWHM (Å^{-1})	V(Å^3)
Low strain spinel	8.3899	8.3851	8.3882	-6×10^{-4}	0.001	590.2
High strain spinel	8.3926	8.3823	8.3892	-12×10^{-4}	0.001	590.4
[Ref. [17]]	8.3880	8.3780	8.3850	-11×10^{-4}	0.008	589.5

distortion is associated with a magnetostriction effect. Only very minor differences between the magnetic moments in the two unit cells are expected.

These observations reveal a more complex structure than that reported by Yang and Ren [17], which is the most detailed structural study available, where only a single spinel phase was found for CFO. This difference is most likely due to the order of magnitude lower resolution in those experiments ($\varepsilon_r = 5 \times 10^{-4}$), which would not allow resolving the peak splitting in the low- and high-strain structure (as also evidenced by the reported peak widths; see Table I). Furthermore, the lattice constant a_0 in the paramagnetic state, which can be deduced from the tensor of the lattice distortion [8,17], is also found to be slightly bigger than that obtained in the previous measurements [17], which may be likewise caused by the higher precision of our study.

MOKE microscopy images of the (111) surface [Fig. 2(a)], obtained in the absence of an external magnetic field and in the remanent state, reveal a very complex magnetic microstructure consisting of magnetic microdomains with six possible orientations of the spontaneous magnetization [see the inset of Fig. 2(a)]. These magnetic microdomains are oriented along the [100], [010], and [001] crystallographic directions, are present in equivalent proportions, and seem to correspond to the $A1/A2$, $B1/B2$, and $C1/C2$ crystallographic domains, respectively. The microdomains are separated by 90° and 180° domain walls oriented at 60°/120° to each other. The latter results from the projection of the {100} directions (i.e., the magnetic easy axis of the material) onto the (111) surface. 180° domain walls with an antiparallel magnetization in neighboring domains [as schematically depicted in green in Fig. 3(a)] are parallel to the {100} planes; 90° domain walls, where the magnetization is perpendicular to each other, are preferentially oriented parallel to the {101} planes [indicated in blue in Fig. 3(a)]. This picture is also supported by MOKE images of the (001) surface of the crystal [Fig. 2(b)].

Interestingly, the lattice match of the low- and the high-strain CFO phase is perfect along the [101] direction, with the length of the diagonal $d_{[101]} = \sqrt{a_1^2 + c_1^2} = \sqrt{a_2^2 + c_2^2} = 11.8617$ Å. Based on this observation, we propose a model where at $H = 0$ the crystal consists of an equal fraction of high- and low-strain domains that are separated by {101} domain boundaries [shown schematically in Fig. 3(b)]. In this arrangement the neighboring microdomains have to be slightly tilted by an angle α in order to have a perfect diagonal match at the domain boundary. The latter is essential to minimize the stress at the domain wall [27]. As shown in Fig. 2(c), this

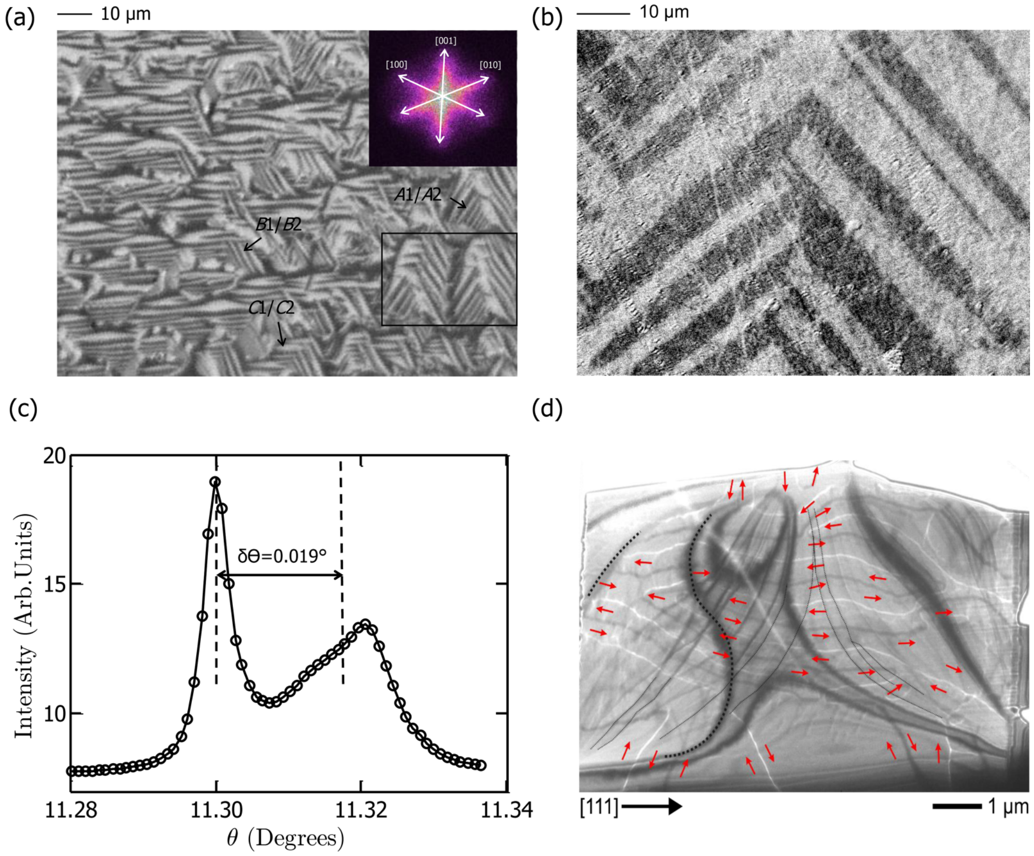

FIG. 2. MOKE microscope images of the magnetic microdomains on the (a) (111) surface and (b) (100) surface of CFO, showing 90° and 180° microdomain walls. The inset in (a) is the Fourier transformation of the MOKE image. (c) Rocking curve across the {400} CFO Bragg reflection measured during the application of an external magnetic field $H = 3.8$ kOe. The two peaks correspond to the axial domains. (d) Fresnel image (defocus +1 mm) of the CFO (112) plane, showing magnetic microdomain walls (thin black and white lines) that run perpendicular to the (111) surface of the CFO crystal. The proposed orientations of the magnetic moments within the domains are indicated by red arrows. The broad dark lines are bending contours, originating from the warp of the 100 nm thick sample.

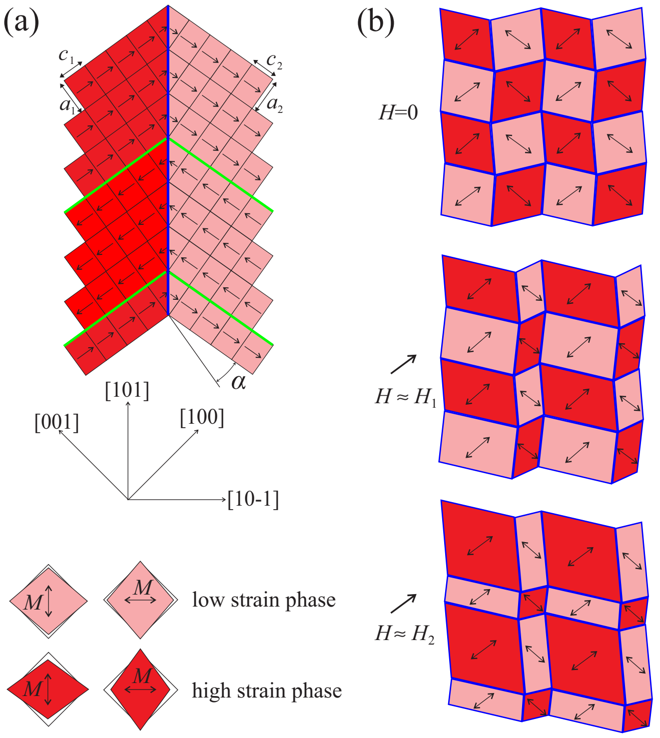

FIG. 3. Schematic illustration of the crystallographic domain microstructure. (a) Structure of the 180° domain walls parallel to the {100} planes (green lines) and the 90° domain walls parallel (blue line) to the {101} planes. (b) Larger scale arrangement of the low- and high-strain spinel domains as a function of the external magnetic field intensity *H*. Black arrows indicate the direction of the magnetization.

splitting of the domain orientations can be directly observed in rocking curves of the Bragg reflections. This measurement was performed with a magnetic field of $H = 2.6$ kOe, where only those high- and low-strain domains with the *c* axes parallel to the field direction remain (see below). The expected angle for a perfect {101} boundary between those domains is $\alpha = a\,\tan(a_1/c_1) + a\,\tan(c_2/a_2) - 90^\circ = 0.019^\circ$, which is in excellent agreement with the experimental observations. It should be mentioned that the true domain distribution is probably less regular and more complex than that shown in Fig. 3(b). In particular, it will require a three-dimensional (3D) rather than a planar arrangement of the six different spinel domains (e.g., formed by quasirhombododecaedrical domains). Nevertheless, the boundary conditions can still be largely fulfilled. Following Yang and Ren [17], we propose that the magnetization is oriented parallel to the *c* axes and identify the 90° domain walls to be parallel to the {101} planes in the MOKE images with domains between the low- and high-strain phase. However, the observed 180° magnetization domains parallel to the {100} planes are probably not accompanied by a change from low to high strain, because of the poor lattice mismatch of the two CFO phases along this direction. Instead, they are assigned to a domain substructure within a single high- or low-strain domain, respectively, as indicated in Fig. 3(a). Since the magnetostriction only depends on the absolute value of *H*, such 180° boundaries are not associated with lattice mismatch and thus do not carry an elastic energy contribution. Constructing a configuration of the six domain types is a very complex geometric problem, since it requires making a 3D arrangement composed of blocks with two different triclinic unit cells. Furthermore, there is the possibility that the real domain structure is hierarchical on several length scales: On the smallest (submicrometer) scale we have the 180° domains, on intermediate length scales we have an arrangement as in Fig. 3 (i.e., a 2D tiling), and on very large length scales we have areas of such tiling along the three symmetrically equivalent directions (at the boundaries between those areas we then would not have any matching). This arrangement may also work in 3D, but providing a rigorous model is difficult due to geometric complexity.

Complementary images of the magnetic domain structure were obtained by Lorentz microscopy, using a <100 nm cross section cut perpendicular to the (111) surface. A Fresnel image of the CFO single crystal, showing the magnetic domain walls (visible as bright and dark lines) and the corresponding magnetic orientations (indicated by arrows) is shown in Fig. 2(d). The stripelike 180° domains are clearly visible. Additional contrast lines, running perpendicular to the domain walls and thus perpendicular to the orientation of magnetization, can be interpreted as bend contours related to internal stress and thickness variations of the thinned and slightly warped FIB lamella (examples marked by black dotted lines). Their presence is also observed in TEM bright field images. According to the Fresnel image the orientation of the magnetic domains is following the local stress anisotropy within the CFO material, providing a strong indication that stress and magnetic structure are directly linked in CFO.

The complex domain structure and, more generally, the presence of a high- and a low-strain CFO phase is most likely driven by internal stress, caused by the transition from the cubic paramagnetic to the ferrimagnetic spinel phase. Because spinel domains of all three symmetrically equivalent orientations form simultaneously during the transition, substantial tensile and compressive stresses would emerge at the boundaries should all domains exhibit identical lattice parameters. In this case the sample would exhibit a broad distribution of locally different strains (the boundary strain in related oxide materials was found to extend over several micrometers [20,21,28]). In contrast, the structure as proposed in Fig. 3(b), where domains of a phase with a lattice distortion ε and those with a distortion 2ε alternate and occupy equal volume fractions, allows a uniform strain distribution with complete space filling and thus can accommodate this stress. Our results indicate that the latter is more favorable than the former.

Further insight into the structural transformation underlying magnetostriction was obtained by *in situ* XRD high-resolution studies as a function of the external magnetic field strength. As seen in Fig. 1, with increasing magnetic field, the intensity of peaks *A*1/*B*1 and *A*2/*B*2 corresponding to the transversal crystallographic domains diminishes and the intensity of peaks *C*1 and *C*2 corresponding to axial crystallographic domains is enhanced. We note that in the remanent state (after saturation) the XRD peaks split once again into four peaks with positions and intensities very slightly different from those of the peaks starting at zero field. This reflects the low hysteresis in the CFO magnetization curves.

To understand and determine the magnetostriction behavior more quantitatively, the peaks were fitted with four Gaussian functions for all magnetic fields. Since the integrated intensity of a Bragg peak is directly proportional to the volume of the diffracting material, the volume fraction (ν_i) of each domain can be calculated from the corresponding integrated peak areas I_i via $\nu_i = I_i(H)/\Sigma I_i(H)$ where the index $i = A1$, $B1$, $C1$, $A2$, $B2$, and $C2$. Figure 4(a) shows the volume fractions ν_i of all the domains as a function of magnetic field. The change in intensity that can be explained by two different field-induced reorientation processes of the crystallographic domains [illustrated schematically in Fig. 3(b)]: In the first step, the $A1/B1$ and $A2/B2$ transversal domains are switched to $C1$ and $C2$ axial domains, respectively [Fig. 3(b), $H \approx H_1$]; in the second one almost two thirds of the low-strain ($C2$) axial domains are converted to high-strain ($C1$) axial domains [Fig. 3(b), $H \approx H_2$] where H_1 and H_2 correspond to the values of the magnetic field where the half of domains are switched, respectively. At values above the saturation field of ≈4 kOe, the volume fraction of the high-strain axial domains is seven times larger than that of the low-strain axial domains while the transversal domains have almost disappeared. This behavior can be explained in terms of the magnetic anisotropy energy in the tetragonal phase, which preferentially aligns the c_1 axis of the tetragonal structure (i.e., the direction of the local magnetization) parallel to the magnetic field direction. In other words, the $C1$ axial domains are more energetically stable in a magnetic field parallel to the z direction [29].

The domain sizes of each phase are calculated from the full width at half maximum (FWHM) of the Bragg peaks [30] for the directions parallel (L_{para}) and perpendicular (L_{perp}) to the x-ray scattering vector (i.e., magnetic field), respectively, as shown in Figs. 4(b) and 4(c). We obtain domain sizes in the range of 0.8–3 μm depending on the phase and orientation. Additionally, we estimate a magnetic domain size of 1–3 μm from the MOKE observations, providing excellent agreement. With increasing magnetic field, the domain sizes L_{para} and L_{perp} corresponding to the transversal crystallographic domains $A1/B1$ and $A2/B2$ diminish and those of $C1$ and $C2$ corresponding to axial crystallographic phases increase. In the case of $C2$ we observe a drop for the high-field range [Fig. 4(c)]. This agrees with the intensity behavior and is consistent with a field-induced reorientation process of the transversal crystallographic domains to axial domains.

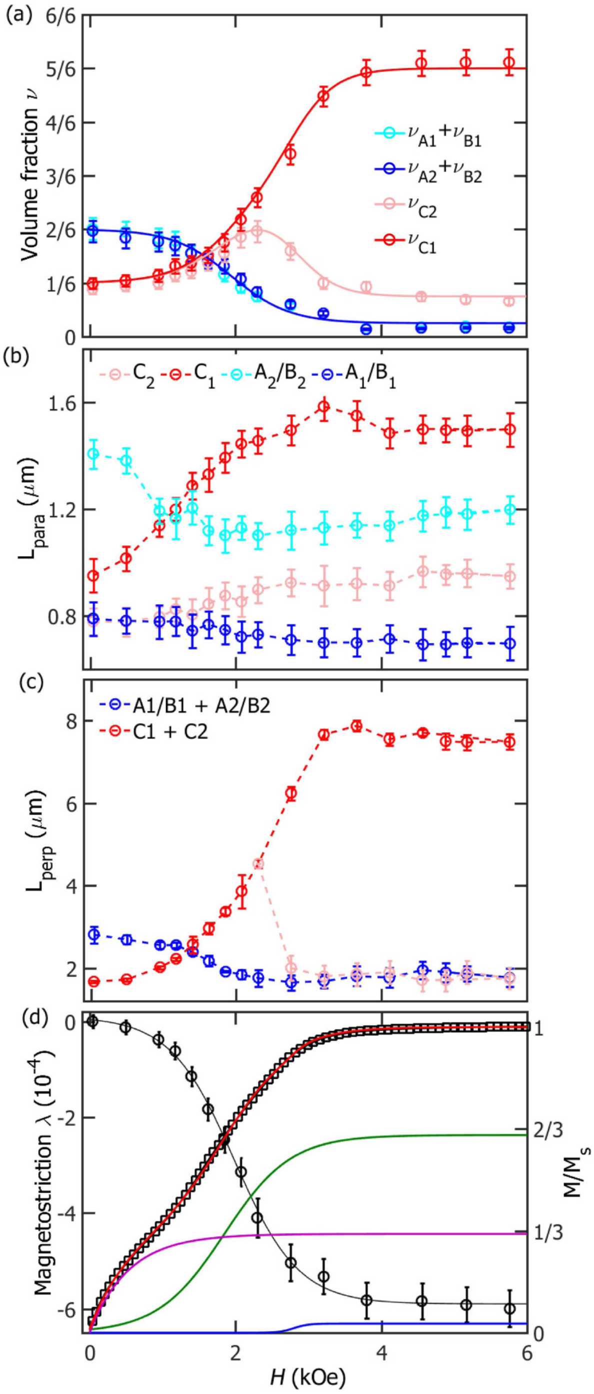

FIG. 4. (a) Magnetic field dependence of the volume fractions of the axial ($C1$, $C2$) and transversal ($A1/B1$, $A2/B2$) domains of the high- and the low-strain spinel phase. In addition to the experimental values (circles) the best fit of a phenomenological model (solid lines) is shown. Magnetic field dependence of the axial ($C1$, $C2$) and transversal ($A1/B1$, $A2/B2$) domain sizes in (b) parallel L_{para} and (c) perpendicular L_{perp} directions to the x-ray scattering vector, respectively. (d) Magnetostriction along [001] (circles) and magnetization (squares) as a function of the strength of an external magnetic field, applied along the [001] direction. In addition, the best fit of the magnetization curve by the model (red line) and the contributions of the two structural reorientation processes (blue and green lines) and the initial polarization of the axial domains via shifting of 180° domain walls (violet line) are shown.

IV. STRUCTURAL DOMAIN MODEL

The structural changes can be described by a simple phenomenological model using a combination of two functions for the volume fractions of the axial domains [$\nu_{C1}(H)$ and $\nu_{C2}(H)$] and only one function for those of the transversal domains [$\nu_{A1}(H), \nu_{B1}(H), \nu_{A2}(H)$, and $\nu_{B2}(H)$]. We adapt a sigmoid function with three parameters as used previously by others [31,32] to describe the magnetostriction behavior,

$$\nu_{C1}(H) = \nu_0 + f_1(H) + f_2(H), \tag{1a}$$

$$\nu_{C2}(H) = \nu_0 + f_1(H) - f_2(H), \tag{1b}$$

$$\nu_{A1}(H) = \nu_{B1}(H) = \nu_{A2}(H) = \nu_{B2}(H) = \nu_0 - \frac{f_1(H)}{2}, \tag{1c}$$

$f_1(H) = \nu_1[1 + e^{-\frac{H-H_1}{\Delta H_1}}]^{-1}$ and $f_2(H) = \nu_2[1 + e^{-\frac{H-H_2}{\Delta H_2}}]^{-1}$ describe the two transition processes, ν_0 is the volume fraction, and $\nu_0 + \nu_1 + \nu_2$ is the saturation volume fraction. The functions $f_1(H)$ and $f_2(H)$ provide a phenomenological description of the magnetostriction behavior inside the magnetic material as a function of the magnetic field H and include the magnetic anisotropy and the magnetization reversal process. Here, H_1 and H_2 are the values of the magnetic field where $f_1(H)$ and $f_2(H)$ reach half of the volume fractions ν_1 and ν_2, respectively, and the parameters ΔH_1 and ΔH_2 are the characteristic widths. The best fit of the experimental data [solid lines in Fig. 4(a)] to this model was obtained with an initial volume fraction $\nu_i(0) = \nu_0 = 1/6 \pm 0.01$, supporting again the isotropic domain orientation at $H = 0$, volume fractions $\nu_1 = 15/48 \pm 0.02$ and $\nu_2 = 17/48 \pm 0.02$, transition widths $\Delta H_1 = 0.40 \pm 0.02$ kOe and $\Delta H_2 = 0.10 \pm 0.01$ kOe, and characteristic magnetic field values of the two transitions of $H_1 = 1.95 \pm 0.05$ kOe and $H_2 = 2.80 \pm 0.05$ kOe. Therefore, $\nu_{A1} = \nu_{B1} = \nu_{A2} = \nu_{B2} = 1/96$, giving a total volume fraction of 2/48 for the transversal domains in saturation ($H \gg H_1$).

The H-field-induced change in the volume fraction of switched domains of type i is given by $\Delta\nu_i(H) = \nu_i(H) - \nu_i(0)$. The values of the volume fraction and the lattice distortion can be used to calculate the magnetostriction $\lambda(H)$ via

$$\lambda(H) = [\varepsilon_{\mathrm{hs},1}(H) + \varepsilon_{\mathrm{ls}}(H)]\frac{[\Delta\nu_{C1}(H) + \Delta\nu_{C2}(H)]}{2} + \varepsilon_{\mathrm{hs},2}(H)\frac{[\Delta\nu_{C1}(H) - \Delta\nu_{C2}(H)]}{2}, \qquad (2)$$

with $\varepsilon_{\mathrm{hs},1}(H) = \frac{c_1(H)}{a_1(H)} - 1$, $\varepsilon_{\mathrm{ls}}(H) = \frac{c_2(H)}{a_2(H)} - 1$, and $\varepsilon_{\mathrm{hs},2}(H) = \frac{c_1(H)}{c_2(H)} - 1$.

Using Eq. (1), $\lambda(H)$ can also be calculated from the phenomenological model:

$$\lambda(H) = [\varepsilon_{\mathrm{hs},1}(0) + \varepsilon_{\mathrm{ls}}(0)]f_1(H) + \varepsilon_{\mathrm{hs},2}(0)f_2(H). \qquad (3)$$

The resulting magnetostriction curve is shown in Fig. 4(d). With increasing field the CFO sample is compressed and approaches a nearly constant value of -6×10^{-4} at fields of about 4 kOe. This value is in agreement with literature values obtained by macroscopic measurements of the magnetostriction [1]. Obviously, the macroscopic magnetostriction curve does not reflect the complex two-stage process of the structural change in the material, which is caused by the significant overlap of the two processes. This illustrates the need for detailed structural studies in order to understand the microscopic origin of magnetostriction.

In addition, Fig. 4(d) displays the magnetization curve of the sample, which likewise indicates a multistep process. The magnetization change at low fields ($H < 1$ kOe), where the reorientation of the structural domains is negligible, is attributed to a polarization of the $C1$ and $C2$ domains, and is most probably due to the $\{100\}$-oriented 180° domain wall propagation. This process does not involve structural changes. The subsequent increase in magnetization can be clearly associated with the domain reorientation processes found in the XRD experiments. This is evident for the first structural transition, where the $A1/B1$ and $A2/B2$ domains are converted into $C1$ and $C2$ domains, respectively. Considering that the magnetization within the domains is along the $\boldsymbol{c}$ axes, the growth of the axial at cost of the transversal domains should be accompanied by a proportionate change in magnetization. For the second transition, where the low-strain domains are switched to high-strain domains, the influence on the magnetization is less evident. Nevertheless, the magnetization may further increase also in this regime, if the local magnetization of high-strain domains (M_{C1}) is larger than that of the low-strain domains (M_{C2}).

This microscopic model is validated by quantitatively describing the magnetization curve taking into account the results of the structural analysis. For this we employ a model equation that—in accordance with the experimental data—assumes identical volume fractions of all domains at $H = 0$:

$$M(H)/M_s = \tfrac{1}{3}\left(1 - \tfrac{1}{2}r\right)\left(1 - e^{-\frac{H}{\Delta H_0}}\right) + \tfrac{2}{3}\left(1 - \tfrac{1}{2}r\right)f_1(H) + \tfrac{1}{2}r\, f_2(H), \qquad (4)$$

where the first term describes the initial polarization of the axial domains occurring at a characteristic field ΔH_0, the functions $f_1(H)$ and $f_2(H)$ are identical to those in Eq. (1), and $r = (M_{C1}\text{-}M_{C2})/M_{C1}$ corresponds to the relative change in magnetization upon switching of $C2$ in $C1$ domains. Fitting the experimental magnetization curve with this expression, using the values of the fit to the structural data for the parameters of $f_1(H)$ and $f_2(H)$, and only r and ΔH_0 as free parameters, we obtain excellent agreement. The corresponding r and ΔH_0 values of the best fit [Fig. 4(d), red solid line] are 0.064 ± 0.003 and 0.53 ± 0.01 kOe, respectively. This implies that the magnetization in the high-strain spinel is slightly larger than that in the low-strain structure, which explains the driving force of the second structural transition.

That magnetization reversal occurs via switching of structural domains rather than the coherent rotation of magnetic moments is also supported by the saturation field, which is half the ideal magnetic anisotropy field $H_A = H_E + H_F \approx 9.1$ kOe, where H_E and H_F are the magnetoelastic and magnetostatic anisotropy fields [calculated using $H_E = -3\varepsilon_s(c_{11}\text{-}c_{12})(c\text{-}a)/a_0/M_S \approx 7.6$ kOe with the saturation magnetostriction $\varepsilon_s = -6 \times 10^{-4}$, the elastic components of the stiffness tensor $c_{11} = 2.7 \times 10^{12}\,\mathrm{dyn/cm^2}$ and $c_{12} = 1.06 \times 10^{12}\,\mathrm{dyn/cm^2}$, and $H_F = 4\pi N M_S \approx 1.5$ kOe with $N \approx 1/3$ being the demagnetizing factor [33,34]]. Magnetization reversal via motion of 90° twin domain walls has already been observed in NiMnGa magnetic shape memory alloys [35]. However, the field-induced structural transition from a low- to a high-strain structure and the associated increase in magnetization has not been reported previously.

V. CONCLUSIONS

Our direct x-ray studies of field-induced strain demonstrate that the magnetostriction of CFO results from the switching of structural domains via a complex two-step mechanism. The very high resolution of these measurements allows us to resolve the presence of low- and high-strain domains of a tetragonal spinel structure which coexist at equal volume fractions in the absence of an external field. The structural observations can be rationalized by a folding of the crystal lattice into alternating microdomains during the paramagnetic-ferrimagnetic phase transition in order to release internal stress. The magnetic field-induced reorientation of these domains is responsible for the large magnetostriction of this material, analogous to the mechanism found in ferroelectrics and ferroelastic materials [36]. Using a simple phenomenological model, both the field-dependent magnetostriction and magnetization can be described, providing clear evidence that magnetic and crystallographic domains are directly connected. In the resulting scenario, first domains oriented in the direction of the field are polarized, followed by a reorientation of the perpendicularly oriented domains in the field direction and, eventually, conversion of the low-strain spinel domains into the high-strain structure. The latter seems to be driven by a 6.4% increase in the magnetization of the high-strain spinel. Magnetostriction in other ferro- and ferrimagnetic materials likely will occur via similar microscopic mechanisms.

ACKNOWLEDGMENTS

We acknowledge the financial support by the Deutsche Forschungsgemeinschaft via the collaborative research centre SFB 855 and the National Basic Research Program of China (Grant No. 2012CB619404). We thank ESRF and Diamond Light Source for access and the staff of XMaS and I16 for the support during the experiments.

---

[1] R. M. Bozorth, E. F. Tilden, and A. J. Williams, Phys. Rev. **99**, 1788 (1955).
[2] R. W. McCallum, K. W. Dennis, D. C. Jiles, J. E. Snyder, and Y. H. Chen, Low Temp. Phys. **27**, 266 (2001).
[3] D. Fritsch and C. Ederer, Phys. Rev. B **86**, 014406 (2012).
[4] M. Fiebig, J. Phys. D **38**, R123 (2005).
[5] N. A. Spaldin and M. Fiebig, Science **309**, 391 (2005).
[6] R. Ramesh and N. A. Spaldin, Nat. Mater. **6**, 21 (2007).
[7] J. R. Hattrick-Simpers, L. Y. Dai, M. Wuttig, I. Takeuchi, and E. Quandt, Rev. Sci. Instrum. **78**, 106103 (2007).
[8] E. Du Trémolet de Delacheisserie, *Magnetostriction: Theory and Applications of Magnetoelasticity* (CRC Press, Boca Raton, FL, 1993).
[9] K. A. Schönau, M. Knapp, H Kungl, M. J. Hoffmann, and H. Fuess, Phys. Rev. B **76**, 144112 (2007).
[10] J. Y. Kim, L. Yao, and S. Van Dijken, J. Phys.: Condens. Matter **25**, 082205 (2013).
[11] L. X. Zhang and X. Ren, Phys. Rev. B **71**, 174108 (2005).
[12] J. H. Park, J. H. Lee, M. G. Kim, Y. K. Jeong, M. A. Oak, H. M. Jang, H. J. Choi, and J. F. Scott, Phys. Rev. B **81**, 134401 (2010).
[13] Z. Wang, Y. Yang, R. Viswan, J. Li, and D. Viehland, Appl. Phys. Lett. **99**, 043110 (2011).
[14] J. J. Yang, Y. G. Zhao, H. F. Tian, L. B. Luo, H. Y. Zhang, Y. J. He, and H. S. Luo, Appl. Phys. Lett. **94**, 212504 (2009).
[15] C. W. Nan, G. Liu, Y. Lin, and H. Chen, Phys. Rev. Lett. **94**, 197203 (2005).
[16] C.-W. Nan, G. Liu, and Y. H. Lin, Appl. Phys. Lett. **83**, 4366 (2003).
[17] S. Yang and X. Ren, Phys. Rev. B **77**, 014407 (2008).
[18] M. Kriegisch, W. Ren, R. Sato-Turtelli, H. Müller, R. Grössinger, and Z. Zhang, J. Appl. Phys. **111**, 07E308 (2012).
[19] J. X. Zhang, J. Y. Dai, L. C. So, C. L. Sun, C. Y. Lo, S. W. Or, and H. L. W. Chan, J. Appl. Phys. **105**, 054102 (2009).
[20] R. C. Rogan, N. Tamura, G. A. Swift, and E. Üstündag, Nat. Mater. **2**, 379 (2003).
[21] A. Pramanick, J. L. Jones, G. Tutuncu, D. Ghosh, A. D. Stoica, and K. An, Sci. Rep. **2**, 929 (2012).
[22] R. C. Kambale, K. M. Song, C. J. Won, K. D. Lee, and N. Hur, J. Cryst. Growth **340**, 171 (2012).
[23] W. H. Wang and X. Ren, J. Cryst. Growth **289**, 605 (2006).
[24] S. D. Brown, L. Bouchenoire, D. Bowyer, J. Kervin, D. Laundy, M. J. Longfield, D. Mannix, D. F. Paul, A. Stunault, P. Thompson, M. J. Cooper, C. A. Lucas, and W. G. Stirling, J. Synchrotron Radiat. **8**, 1172 (2001).
[25] J. McCord, J. Phys. D: Appl. Phys. **48**, 333001 (2015).
[26] T. Von Hofe, N. O. Urs, B. Mozooni, T. Jansen, C. Kirchhof, D. E. Bürgler, E. Quandt, and J. McCord, Appl. Phys. Lett. **103**, 142410 (2013).
[27] B. Meyer and D. Vanderbilt, Phys. Rev. B **65**, 104111 (2002).
[28] C. M. Landis, J. Mech. Phys. Solids **56**, 3059 (2008).
[29] T. Suzuki, M. Katsumura, K. Taniguchi, T. Arima, and T. Katsufuji, Phys. Rev. Lett. **98**, 127203 (2007).
[30] B. E. Warren, *X-ray Diffraction* (Addison-Wesley, Reading, MA, 1969).
[31] D. X. feng, G. X. Chun, Q. Min, and J. Ping, Trans. Nonferrous Met. Soc. China **19**, 1454 (2009).
[32] M. Kriegisch, Ph.D. thesis, Technischen Universität Wien, 2012.
[33] A. Lisfi, C. M. Williams, L. T. Nguyen, J. C. Lodder, A. Coleman, H. Corcoran, A. Johnson, P. Chang, A. Kumar, and W. Morgan, Phys. Rev. B **76**, 054405 (2007).
[34] Y. Tsai, H. R. Chen, F. C. Chang, W. C. Tsai, H. M. Cheng, Y. M. Cheng, Y. H. Chu, C. H. Lai, and W. F. Hsieh, Appl. Phys. Lett. **102**, 132905 (2013).
[35] Y. W. Lai, N. Scheerbaum, D. Hinz, O. Gutfleisch, R. Schäfer, L. Schultz, and J. McCord, Appl. Phys. Lett. **90**, 192504 (2007).
[36] X. Ren, Nat. Mater. **3**, 91 (2004).